UC Berkeley
UC Berkeley Previously Published Works

Title

Electronic descriptors for dislocation deformation behavior and intrinsic ductility in bcc high-entropy alloys

Permalink

https://escholarship.org/uc/item/1c44h9br

Journal

Science Advances, 10(38)

ISSN

2375-2548

Authors

Borges, Pedro PPO

Ritchie, Robert O

Asta, Mark

Publication Date

2024-09-20

DOI

10.1126/sciadv.adp7670

Copyright Information

Peer reviewed

MATERIALS SCIENCE

Electronic descriptors for dislocation deformation behavior and intrinsic ductility in bcc high-entropy alloys

Pedro P. P. O. Borges[1,2]*, Robert O. Ritchie[1,2], Mark Asta[1,2]*

Controlling the balance between strength and damage tolerance in high-entropy alloys (HEAs) is central to their application as structural materials. Materials discovery efforts for HEAs are therefore impeded by an incomplete understanding of the chemical factors governing this balance. Through first-principles calculations, this study explores factors governing intrinsic ductility of a crucial subset of HEAs—those with a body-centered cubic (bcc) crystal structure. Analyses of three sets of bcc HEAs comprising nine different compositions reveal that alloy chemistry profoundly influences screw dislocation core structure, dislocation vibrational properties, and intrinsic ductility parameters derived from unstable stacking fault and surface energies. Key features in the electronic structure are identified that correlate with these properties: the fraction of occupied bonding states and bimodality of the d-orbital density of states. The findings enhance the fundamental understanding of the origins of intrinsic ductility and establish an electronic structure–based framework for computationally accelerated materials discovery and design.

INTRODUCTION

Metallic alloys containing multiprincipal elements, often referred to as high-entropy alloys (HEAs), have inspired extensive research due to an almost unlimited design space for optimizing mechanical properties for structural and functional applications (*1*, *2*). A specific class of these materials crystallizes as single-phase body-centered cubic (bcc) solid solutions (*3*) and is composed primarily of refractory transition metals (V, Nb, Ta, Cr, Mo, and W) (*4*, *5*), group IV elements (Ti, Zr, and Hf) (*6*), and Re (*7*, *8*). Depending on composition, bcc HEAs have been demonstrated to show outstanding mechanical properties, spanning exceptional resistance to thermal softening (*5*), remarkably high fracture toughness (*9*, *10*), and retained tensile ductility at cryogenic temperatures (*11*, *12*). Concerning damage tolerance in particular, it is appreciated that the unique behavior of HEAs stems from a complex synergy of deformation mechanisms (*11*, *13*, *14*). However, the link between these mechanisms and alloy chemistry remains incompletely understood, presenting a situation that has hindered accelerated discovery in the vast compositional space available.

With the aim of providing these guidelines, theoretical and computational work has improved understanding of the underlying physics controlling dislocation slip in bcc HEAs. These efforts have been focused on clarifying strengthening effects (*15*), where details of the local chemistry are shown to induce fluctuations in the energy landscape (*16*) and distortions of the bcc lattice (*17*, *18*), both leading to rugged dislocation lines (*19*) that enhance the HEA strength (*20*). Ductility is, however, less understood. Factors such as electron per atom ratio have shown correlations over a subset of the composition space but are not able to explain the breadth of experimental observations (*21*–*23*). At the atomic scale, where properties of screw dislocations fundamentally influence deformation mechanisms (*24*–*28*),

density functional theory (DFT) calculations have revealed that the HEA composition can alter the ground-state core configuration with respect to elemental bcc metals, specifically inducing core asymmetry (*19*, *28*, *29*), which has been argued to increase the number of available planes for atomistic gliding (*30*, *31*). Nonetheless, comprehensive physical interpretations for these phenomena, at the fundamental level of the electronic structure, a goal of the present work, have not yet been proposed.

Through explicit DFT calculations of the core structure and vibrational properties of screw dislocation cores, as well as unstable stacking fault (USF) and surface energies, the present work identifies a fundamental correlation between synergies of dislocation properties and intrinsic ductility parameters that are linked to features in the bulk electronic structure. In detail, it is demonstrated that either bond strength softening or bimodality suppression reflected in the bulk electronic density of states (DOS) correlates with dislocation core asymmetry, soft vibrational modes that can increase equilibrium kink densities, and intrinsic ductility reflected by the Rice criterion. These findings appreciably advance the understanding of the chemical factors influencing slip and ductility and provide a relatively efficient electronic structure–based framework for computationally accelerating design of bcc HEAs with optimal balance of strength and damage tolerance.

RESULTS

We primarily focus on two families of bcc HEAs: (i) NbTaMo, NbTaMoW, and NbTaMoWV; and (ii) NbTaTi, NbTaTiHf, and NbTaTiHfZr—all modeled as random solid solutions using the special quasirandom structure (SQS) approach (*32*), as described in Materials and Methods. Our aim is not only to investigate the effect of the total number of elements but also to highlight different phenomena observed in the (i) refractory bcc HEAs [i.e., composed exclusively by refractory metals of group V (V, Nb, Ta) and group VI (Mo and W) elements] and (ii) group IV–containing bcc HEAs [i.e., with a large group IV (Ti, Zr, and Hf) element concentration]. To

[1]Materials Sciences Division, Lawrence Berkeley National Laboratory, Berkeley, CA 94720, USA. [2]Department of Materials Science and Engineering, University of California, Berkeley, CA 94720, USA.
*Corresponding author. Email: pedro_borges@berkeley.edu (P.P.P.O.B.); mdasta@berkeley.edu (M.A.)

extend the discussion to an even larger set of bcc HEAs, we also examine the MoReW, which has been shown experimentally to feature ductile behavior at room temperature (*8*).

The following subsections are organized as follows. We first examine the properties of screw dislocations in the bcc HEAs presented above, focusing on the dislocation core ground-state configuration, vibrational properties relevant to dislocation line profiles, and generalized stacking fault energy. We establish correlations between these properties and deformation mechanisms experimentally observed in bcc HEAs and extend the analysis to examine widely used intrinsic ductility criteria [Pugh ratio (*33*), Rice-Thomson (*34*), and Rice (*35*)]. Further, we investigate the underlying details of the electronic structure controlling these properties, defining two local electronic descriptors to perform this analysis: fraction of occupied bonding states and featuring bimodality of d-orbital DOS.

1/2 ⟨111⟩ screw dislocation core ground-state configuration

We consider first the ground-state core configuration of screw dislocations with Burgers vector $\vec{b} = a_0 / 2 \langle 111 \rangle$, a property that critically controls the atomistic glide of these dislocations (*30*). Previous theoretical studies have proposed two types of core structure: symmetric or asymmetric (*30, 36–38*).

As proposed in (*39*), the so-called core polarization (*p*) allows to quantitatively assess the symmetry of the core. This parameter is defined as

$$p = \frac{|d_{BC} - d_{AB}| + |d_{DE} - d_{CD}| + |d_{FA} - d_{EF}|}{b} \quad (1)$$

where d_{xy} (x, y = A, B, C, D, E, or F) is the relative displacement between two neighboring ⟨111⟩ atomic columns as indicated in Fig. 1A and b is the magnitude of the Burgers vector (i.e., $b = |\vec{b}|$). With such a definition, ideally symmetric or fully asymmetric cores lead to $p = 0$ or 1, respectively. We use this parameter to quantify the degree of core polarization in the bcc HEAs below.

DFT calculations have established that elemental bcc transition metals (V, Nb, Ta, Mo, and W) show symmetric cores (*40–43*). In agreement with these studies, as shown in Fig. 1A, we obtain the symmetric core as the ground-state structure in elemental bcc Nb, referred to as the easy core configuration (*43, 44*). We also examine the asymmetric core in pure bcc Nb for the sake of comparison (Fig. 1B). As described in (*39, 45*), the asymmetric core is obtained from the symmetric core by applying correlated displacements along ⟨111⟩ on the atomic columns indicated in Fig. 1A, followed by a constrained structural relaxation. Figure 1B shows that the asymmetric core spreads in three ⟨112⟩ directions on {110} planes.

The features shown in Fig. 1 (A and B) allow a clear distinction between symmetric and asymmetric cores. Specifically, the differential displacements (*36*) of the second nearest-neighbor shell (A → B → C → D → E → F path) of the core correlate with the Burgers circuit in the case of the symmetric core, which can be regarded as six generalized splittings into fractional dislocations with screw components $\vec{b} / 6$ (*37, 45*). In the case of the asymmetric core, however, the second nearest-neighbor shell differential displacements do not correspond to a closed loop, reflecting three fractional dislocations with screw components $\vec{b} / 3$ (*37, 45*). Moreover, the high dislocation density around the symmetric core shown by the Nye tensor (*46*) evidences its compactness; in contrast to the asymmetric core, where the diffuseness of the Nye tensor reflects core spreading.

We focus next on the bcc HEAs (Fig. 1, C to I). For each system, we investigate the core structure in five different SQS models to certify that the configurations presented in Fig. 1 are representative of the studied materials. This strategy allows to sample different chemical environments within the dislocation core, which mimics corresponding fluctuations along the dislocation line. The core polarization parameters presented in Fig. 1 are averaged over these five configurations, and the variations across different SQS models are presented in text S2. In Fig. 1, we plot the core configurations with computed polarization parameters closest to the average value for each HEA composition, and the specific values of *p* for the configurations shown are presented in table S2. In addition, we systematically verify that both dislocations of the dipole and both layers of the cell relax to equivalent positions, i.e., according to the symmetry of the bcc lattice (see Materials and Methods for details).

Figure 1 (D to F) shows that the set of refractory bcc HEAs (NbTaMo, NbTaMoW, and NbTaMoWV, respectively) shows almost ideally symmetric cores. As illustrated by the differential displacements and Nye tensor, the core structure is essentially compact, consistent with previous DFT calculations (*16, 28*). Small magnitudes of the polarization parameter mainly arise from fluctuations in the energy landscape observed by the dislocation. Specifically, these fluctuations are driven by chemical complexity (*16, 47*) and should become more important as the number of elements with widely differing Peierls barriers increases. For instance, DFT calculations in (*43*) show that the Peierls barrier is approximately equal to 25, 35, 37, 50, and 82 meV/*b* for V, Nb, Ta, Mo, and W, respectively. In this sense, V and W additions to NbTaMo might be expected to enhance the roughness of the dislocation energy landscape. In these situations, the core position might slightly move away from the reference perfectly symmetric configuration to optimize its energy, leading to a small degree of core asymmetry.

In both the MoReW (Fig. 1C) and group IV–containing NbTaTi (Fig. 1G), NbTaTiHf (Fig. 1H), and NbTaTiHfZr (Fig. 1I) bcc HEAs, the ground-state core configuration features substantial asymmetry, as shown by the calculated polarization parameters. We also observe that the core asymmetry is enhanced as the group IV element concentration increases, consistent with prior DFT studies (*19, 28, 29, 48*). We also highlight that increasing core asymmetry due to compositional effects has been observed in W-Re bcc alloys in previous DFT calculations (*31, 49*). To further emphasize different details in the core configuration found in refractory versus group IV element– and Re-containing bcc HEAs, we examine the edge components of screw dislocations and formation volumes, which are presented in text S3.

The type of core structure plays a major role on dislocation mobility. Whereas symmetric cores glide on average in {110} planes (*43, 50*), asymmetric cores have been shown to glide in a zigzag fashion in these planes changing the overall slip plane to {112} (*30*). These results suggest that while dislocation glide should be constrained to the {110} slip system in the refractory HEAs, in the group IV–containing and MoReW HEAs, both {110} and {112} families of planes may be available for dislocation slip. We note that experimental studies have reported 1/2 ⟨111⟩ screw dislocation slip traces along both {110} (*11, 24, 27*) and {112} (*11, 14, 27, 51–54*) in group IV–containing bcc HEAs, with preferred {112} slip in NbTaTiHfZr shown in (*28*).

The more effective participation of {112} slip reflects an appreciable increase in available glide planes, which correlates with
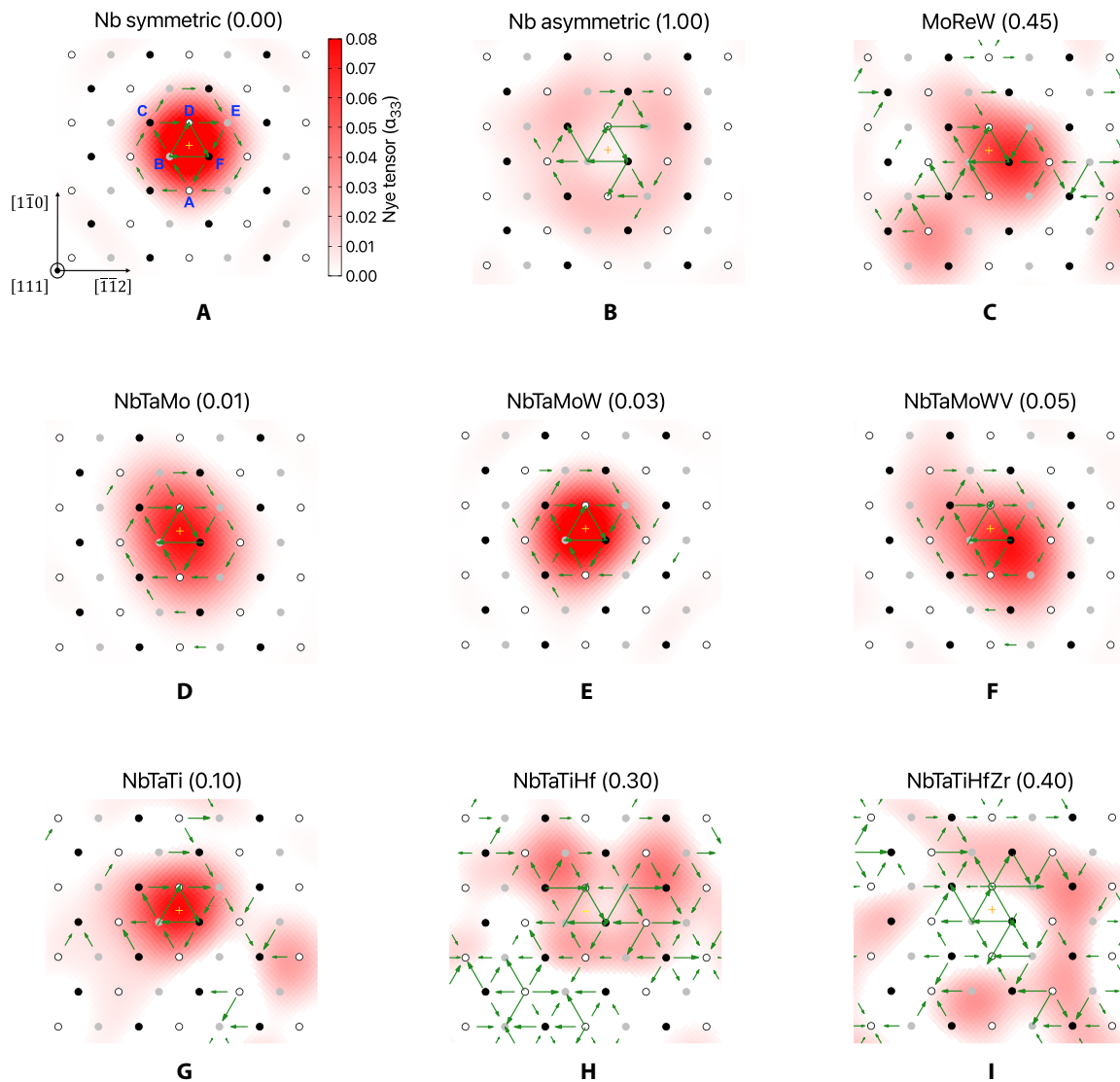
Fig. 1. First-principles calculated core structures for 1/2 ⟨111⟩ screw dislocations in bcc metals and HEAs. (**A**) Symmetric and (**B**) asymmetric core in elemental bcc Nb and ground-state core configuration obtained in the (**C**) MoReW, (**D**) NbTaMo, (**E**) NbTaMoW, (**F**) NbTaMoWV, (**G**) NbTaTi, (**H**) NbTaTiHf, and (**I**) NbTaTiHfZr bcc HEAs. The computed average value of core polarization over five different SQS models for each HEA composition is shown in parentheses. We plot above the core structure with calculated polarization parameters closest to the average value for each HEA, and the specific core polarization of these plots are presented in table S2. The atomic structure is projected in the {111} plane, and white, gray, and black circles indicate original {111} planes in a perfect bulk bcc crystal. Arrows are drawn proportional to the relative displacement normalized by *b*/2 between neighboring ⟨111⟩ atomic columns along the Burgers vector direction and are omitted if they are smaller than *b*/12. The contour map shows the screw component of the Nye tensor (α_{33}). Both differential displacements and Nye tensor are calculated with respect to ideal bcc lattice sites. Crosses indicate the reference perfectly symmetric dislocation core position.

improvements in room-temperature ductility observed in experiments. Specifically comparing refractory and group IV–containing bcc HEAs, the peak true strain (ε_p) measured in compression tests in the NbTaMoWV is smaller than 3% (*5*), in stark contrast to the NbTaTiHfZr where $\varepsilon_p > 50\%$ (*6*). These differences are also observed in the three- (*55*, *56*) and four-component (*5*, *57*) bcc HEAs to a degree that is enhanced as the group IV element concentration increases. These trends in increasing ductility with increasing group IV element concentration correlate with the increasing propensity for core polarization in the present calculations. We highlight that analogous interpretations have been proposed to explain ductilization

observed in related complex concentrated alloys [e.g., W-Re binaries (*31*, *49*) and group IV–containing HEAs (*19*, *28*, *29*)]; specifically, core asymmetry shown by DFT studies correlates with experimental observations of preferred {112} slip (*58*, *59*) and suggests improvements in ductility.

We consider next the correlation of local lattice distortions (LLDs) and core structure. Here, we define LLDs as the average magnitude of atomic displacements (in the absence of the dislocation dipole) obtained from the structural relaxation of the ideal bcc crystal: LLDs are calculated using $\langle \mathrm{LLD} \rangle = (1/n) \sum_{i=1}^{n} |\mathbf{r}_i - \mathbf{r}_i^0|$, where $\mathbf{r}_i$ and $\mathbf{r}_i^0$ indicate the coordinates of the *i*th atom obtained after ionic relaxation

and at ideal bcc lattice sites, respectively, and n is the number of atoms in the cell. Computed $\langle LLD \rangle$ values for the materials considered in this work are presented in the Supplementary Materials.

As shown in Fig. 1 [G (NbTaTi), H (NbTaTiHf), and I (NbTaTiHfZr)], we observe pronounced displacements spread in the {111} plane and even far from the core (~10 Å), which introduces substantial perturbation in the calculation of the Nye tensor. These displacements can be understood regarding the average LLD magnitude observed in the bulk in these materials. For instance, $\langle LLD \rangle = 0.13$ Å in the NbTaTiHf (see table S1), which can be as large as the absolute atomic displacements along the screw component produced by the dislocation at the vicinity of the core according to the anisotropic elasticity solution (60). In this sense, we observe that group IV element additions induce appreciable distortions of the bcc lattice and, thus, in the vicinity of the core, which can enhance the degree of core asymmetry found in these materials.

Severe LLDs in group IV–containing bcc HEAs correlate with structural stability (61, 62). Specifically, atomic displacements away from the ideal bcc lattice may be correlated along the ⟨111⟩ direction, reflecting a pronounced softening of the shear modulus along this direction induced by group IV element additions (62). Group VI elements and Re additions by contrast do not induce similar softening of the elastic properties, which is consistent with the observation that they do not induce pronounced distortions of the core.

Note that in (28), the ⟨111⟩ preferred direction for correlated LLDs in group IV–containing bcc HEAs also corresponds to the direction of the Burgers vector of screw dislocations, which may have implications for dislocation mobility. In addition, previous atomistic simulations (19, 63, 64) have shown that increasing LLDs observed in the bulk correlate with decreasing disparity in the relative mobility between edge and screw dislocations in bcc HEAs (63), arising from substantial lattice friction due to chemical disorder observed by edge dislocations (13, 20).

Screw dislocation vibrational properties

We consider next vibrational properties of screw dislocations, which are argued to be relevant to the formation of equilibrium kinks and ultimately to the roughness profile of the dislocation line. Specifically, we compare the lattice vibrations, here referred as vibrational DOS (VDOS), of the bulk and dislocation configurations (i.e., the 270-atom cell without and with the dislocation dipole, respectively, both structurally optimized) to examine the nature of dislocation-induced changes in the vibrational spectra near the core.

Atomic vibrations are computed at the harmonic level, using finite displacement methods within DFT, as described in Materials and Methods. We plot in Fig. 2 the VDOS projected in the atoms in the first and second nearest-neighbor shells of the screw dislocation core (see Fig. 1A) in relaxed bulk and dislocation core ground-state configurations. The core configurations used to calculate the dislocation vibrational properties are those presented in Fig. 1. We focus on the NbTaMoW (Fig. 2A), NbTaTiHf (Fig. 2B), and MoReW (Fig. 2C) systems, which provides a platform to study broader families of bcc HEAs.

We address first the bulk VDOS. In contrast to the vibrational dispersion of elemental crystals, which typically display three broad peaks (65), we observe in Fig. 2 multiple smaller peaks in the HEAs as a result of vibrational broadening due to chemical disorder (see fig. S3) (66, 67). Moreover, we notice that the VDOS of NbTaTiHf features increased weight at lower (softer) frequencies compared to NbTaMoW and MoReW, with its gravity center located at an almost 30% lower value. In addition, we observe that NbTaTiHf shows a small weight at imaginary frequencies. We note that the role of group IV elements on contributing to lower and imaginary frequencies in VDOS is documented in previous DFT studies (28, 62, 68). We present in fig. S4 the atom-type projected VDOS and further discuss in text S5 the underlying mechanisms controlling details of the vibrational spectra.

We consider next dislocation-induced changes in the VDOS. Figure 2 shows that the VDOS for the atoms in the dislocation cores is substantially broadened. This phenomenon is partly attributed to anharmonicity arising from the large strains observed in the vicinity of the core (69). Vibrations in the bulk lattice interact with dislocations via the so-called fluttering mechanism, i.e., an incident vibration induces the dislocation to oscillate and thus also to vibrate (70). As a result, we observe that the dislocation core introduces several additional peaks into the VDOS corresponding to its vibration modes, most evident in the NbTaMoW as shown in Fig. 2A.

Ninomiya (71), as well as related work cited therein, considers the vibrational frequencies of a continuum crystal with a dislocation. The analysis finds that the lowest eigenfrequency for each nonzero wave vector along the dislocation line corresponds to a phonon localized on the dislocation and has a value that is below that of the continuum crystal. In the present calculations, we have verified that this behavior is reproduced in our calculations (see fig. S5). More generally, we observe a noticeable population of
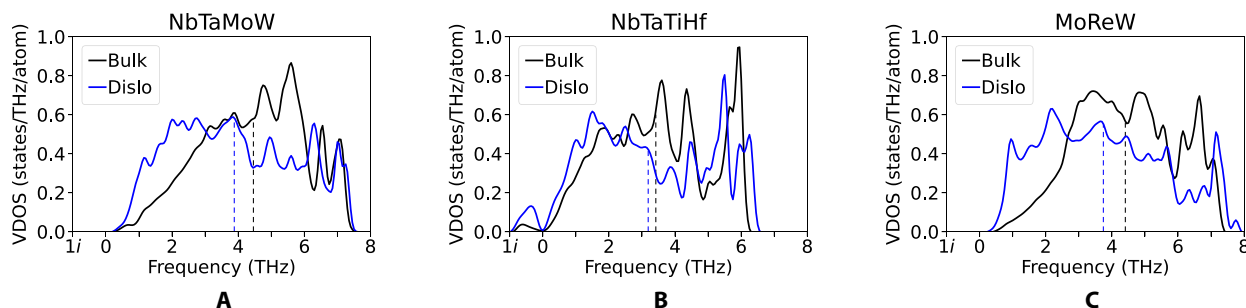

Fig. 2. VDOS projected onto atoms in bulk and in screw dislocation core configurations. VDOS are plotted for the atoms in the first and second nearest-neighbor shells in relaxed structures corresponding to the bulk (black lines) and to dislocation core ground-state (blue lines) configurations obtained in the (**A**) NbTaMoW, (**B**) NbTaTiHf, and (**C**) MoReW bcc HEAs. The core configurations used to calculate the dislocated crystal VDOS are those shown in Fig. 1. Dashed lines indicate the frequency gravity center of respective vibrational spectra.

lower-frequency states induced by the dislocation core leading to a substantial softening of the vibrational spectra, which is reflected in a decrease in the frequency gravity center in both the NbTaMoW and MoReW of about 15%. Even if such an effect is less pronounced ($\approx$7%) in the NbTaTiHf, the frequency gravity center of the group IV–containing HEA is still approximately 25% lower than the other two materials.

These dynamic properties of the dislocation core have potentially important implications in the kink-pair mechanism for dislocation motion. Specifically, the string model (72) considers the dislocation as a line tension on a corrugated substrate (i.e., subjected to a Peierls potential) and predicts that the interaction of dislocations with low-frequency elastic waves may promote the nucleation of kinks. In this sense, the softer vibrational spectra of the dislocated crystal observed in NbTaTiHf, combined with lower energy barriers for kink nucleation (further discussion of kinks in relation to calculations for USFs is given below), should increase the concentration of equilibrium kinks in this alloy. As a result, the dislocation might be expected to adopt a more rugged line profile in the group IV–containing HEAs, consistent with previous atomistic simulations (63). This naturally kinked structure markedly affects the dislocation mobility (73), enhancing cross-slip and cross-kink formation, which has been argued to improve the alloy strength (73).

In addition, we also observe that the screw dislocation core enhances imaginary modes (i.e., $\nu^2 < 0$) in NbTaTiHf. As demonstrated in (62), these modes are intrinsically correlated with LLDs and likely explain the large LLDs observed in the vicinity of the core in the NbTaTiHf but not in the NbTaMoW and MoReW HEAs.

USF energy

We consider next the USF associated with dislocation slip by a Burgers vector $\vec{b} = a_0 / 2 \langle 111 \rangle$. Previous theoretical studies (74, 75) have demonstrated that the USF energy (γ_{us}) is strongly correlated with the energy landscape observed by screw dislocations. In this way, to obtain insight into the energetics controlling the gliding of dislocations considered above, we calculate the γ_{us} values for bcc HEAs considering {110}, {112}, and {123} slip planes from DFT (see Materials and Methods for details). The consideration of high-order planes (i.e., {112} and {123}) is included to examine the interplay of group IV elements and Re additions on the anisotropy of USF energies compared to the reference {110} planes, and the results are argued to be relevant in the context of experimentally reported (13, 27, 28) slip along these high-order planes. The results are shown in Fig. 3. In addition, we also calculate γ_{us} for elemental bcc metals (see table S4)

and include the obtained values for Hf, Ta, and W in Fig. 3 to elucidate alloying effects. In the case of HEAs, we use three different SQS models for each composition and slip plane to calculate γ_{us} and observe that relative differences between maximum and minimum values with respect to the average are smaller than 7% across these SQS models.

Considering pure group V metals (V, Nb, and Ta) as reference (see table S4), Fig. 3 shows that while alloying with group VI elements (Mo and W) leads to an increase in the γ_{us} values, additions of group IV elements (Ti, Zr, and Hf) appreciably lower the USF energy. Specifically, for systems with the same number of components, group IV–containing HEAs (NbTaTi, NbTaTiHf, and NbTaTiHfZr) show γ_{us} values almost three times smaller than refractory HEAs (NbTaMo, NbTaMoW, and NbTaMoWV, respectively) along all studied slip planes. We highlight that these effects of group IV elements on γ_{us} are consistent with previous DFT calculations (64, 76). Further, using the Peierls-Nabarro framework (74, 75), such a decrease in the USF energy should accompany a decrease in the kink-pair formation energy, increasing the nucleation of kinks. In addition, atomistic simulations (77) in elemental bcc metals show that these correlations between γ_{us} and dislocation mobility are observed not only for screw but also for edge dislocations.

We also find that Re additions induce a reduction in the USF energy. Values of γ_{us} obtained for the MoReW HEA are approximately 40% lower than those obtained for elemental W. This Re alloying interplay has been reported by previous DFT studies (31) and is argued to be correlated to screw dislocation core polarization (31, 49). These Re effects on core polarization and USF energy have been suggested to be the underlying ductilization mechanism of W-Re bcc alloys (58, 59).

Figure 3 also shows that the group IV element concentration induces isotropy between high-order slip systems in terms of the USF energy. Whereas γ_{us} is approximately 15 and 30% larger along {112} and {123} than along {110} in the refractory HEAs, these relative differences are smaller than 3 and 6% in group IV–containing HEAs, respectively. As a result, high-order slip plane isotropy combined with lower energy barriers for kink nucleation (see above) may correlate with enhanced dislocation mobility, suggesting improvements in the alloy ductility. We highlight that experimental studies (13, 27, 28) have reported the activation of {112} and {123} glide planes in bcc HEAs with an appreciable concentration of group IV elements.

We note that quantitative methods for calculating the kink pair activation enthalpy have been proposed in the literature (78). Application of this approach in the context of HEAs is challenged by
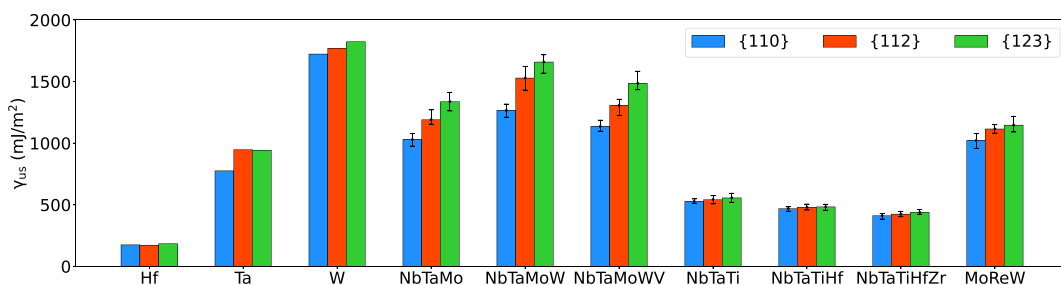
Fig. 3. USF energy (γ_{us}) calculated for {110}, {112}, and {123} slip planes. The blue, red, and green bars indicate the values of γ_{us} for {110}, {112}, and {123} planes, respectively, for elemental bcc Hf, Ta, and W and bcc HEA compositions shown. In the case of HEAs, values are averaged over three different SQS models for each composition and slip plane, with the error bars indicating minimum and maximum calculated values.

the need to sample local fluctuations in the dislocation energy landscape arising from chemical disorder. These calculations are beyond the reach of the present DFT-based approach. In the absence of such an analysis, more qualitative discussions based on USF energies are used here to assess the effects of group IV elements and Re additions on slip behavior.

We end this section with an analysis comparing the DFT-calculated values of γ_{us} obtained here to those computed using the rule of mixtures (ROM) based on values for the elemental bcc metals (see table S4). We find that ROM estimates can substantially underestimate γ_{us}, particularly for {110} planes, being on average 10% (and up to 25% for TaMoReW) smaller than the direct DFT values. Further, the effect of group IV element additions in lowering the anisotropy in γ_{us} values, as found in the DFT calculations, is not reproduced by the ROM estimates. These limitations of the ROM approach are expected because of the nature of the bonding in bcc HEAs. Specifically, Borges *et al.* (*62*) and Tong *et al.* (*79*) discuss substantial charge transfer and rearrangement of the electronic DOS accompanying local relaxations in bcc HEAs. These effects should diminish the accuracy of virtual crystal or rigid band models for the electronic structure, suggesting that simple ROM estimates may be limited in accuracy, as found here.

Intrinsic ductility criteria

The results presented above establish that composition can be tuned to alter screw dislocation properties and γ_{us} in bcc HEAs. Here, we complement this analysis by presenting calculated values for widely used intrinsic ductility parameters. We compare these results with experimental studies that have reported large differences in room-temperature ductility across bcc HEAs. Whereas refractory [NbTaMo (*56*), NbTaMoW (*5*), and NbTaMoWV (*5*)] HEAs have been shown to be brittle, group IV–containing [NbTaTi (*55*), NbTaTiHf (*27*), and NbTaTiHfZr (*6*)] and MoReW (*8*) HEAs have been shown to feature higher ductility. To compare to these experimental findings, we present calculated results for intrinsic ductility parameters obtained for bcc pure elements that have been reported to be intrinsically ductile (V, Nb, and Ta) (*80*) and intrinsically brittle (Mo and W) (*80*) to bcc HEAs with and without group IV elements and Re.

We first assess an elasticity-based ductility criterion. The Pugh ratio, G/B [where G is the isotropic shear modulus, here approximated by Voigt-Reuss-Hill (*81*) averaging of the single-crystal elastic constants, and B is the bulk modulus], represents the competition between plasticity and fracture (*33*). Previous studies (*82*) suggest that materials with $G/B < 0.4$ can be characterized as being typically intrinsically ductile. As shown in Fig. 4A, the Pugh ratio is consistent with improvements in ductility (i.e., smaller G/B ratios) in the group IV–containing HEAs compared to the refractory HEAs, which primarily reflects the pronounced softening of G induced by the group IV element concentration (see the Supplementary Materials). However, Re does not induce an analogous effect on the alloy's elastic properties such that the Pugh ratio remains appreciably large for MoReW, classifying this HEA as brittle alongside elemental Mo and W, in contrast to experimental observations that have shown this material (MoReW) to display notable ductility (*8*). The analysis therefore suggests that elasticity-based criteria are not sufficient to capture the compositional trends in bcc HEAs.

We consider next dislocation-emission ductility criteria. Rice and Thomson (*34*) proposed a theoretical framework where ductility can be regarded as a balance between fracture and nucleation of dislocations at the crack tip. Quantitatively, the Rice-Thomson criterion states that Gb/γ_s, where γ_s is the surface energy and b is the norm of the Burgers vector, controls the ductile nature of materials, with $Gb/\gamma_s < 7.5$ indicating ductile behavior (*34*). Surface energies are calculated for three SQS models for each bcc HEA composition and slip plane, and we verify that variations between minimum and maximum obtained values with respect to the average are smaller than 8% across these SQS models (see table S4). We use average values of γ_s to compute the Rice-Thomson parameters. We consider the surface energy along the {110} slip plane in Fig. 4B and verify that the consideration of {112} or {123} slip planes provides exactly the same trends (see fig. S6).

Figure 4B shows that the shear modulus is the dominant term governing the concentration dependence of Gb/γ_s such that the Rice-Thomson criterion reproduces in general the same trends observed in the Pugh ratio. As a result, while the Rice-Thompson criterion predicts enhanced ductility in the group IV–containing
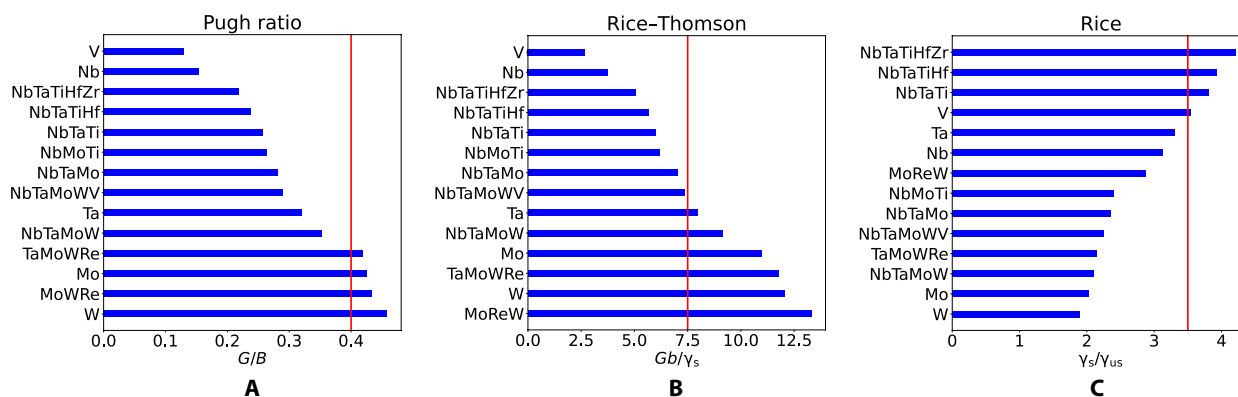
Fig. 4. Calculated values of three intrinsic ductility parameters. (**A**) Pugh ratio. (**B**) Rice-Thomson. (**C**) Rice. In all plots, the material compositions on the vertical axis are presented in ascending ductility order of the corresponding ductility parameter. In (B) and (C), the surface and USF energies are calculated for the {110} slip plane. Red vertical lines indicate ductile to brittle transition thresholds according to reported thresholds for each parameter.

HEAs, it also indicates that the MoReW should be relatively brittle, in contrast to experimental observations (*8*).

We lastly consider the Rice criterion (*35*). In contrast to the Rice-Thomson model, the Rice criterion uses the Peierls approach to analyzing the dislocation nucleation at the crack tip such that the ductility metric becomes γ_s/γ_{us}, where γ_{us} is the USF energy. Quantitative estimations of γ_s/γ_{us} values controlling ductile to brittle transition are very sensitive to the assumptions regarding the crack propagation. As proposed in (*35*), we consider $K_{II} = K_{III} = 0.1K_I$ (where K_I, K_{II}, and K_{III} are the stress intensity factors of modes I, II, and III, respectively), which requires $\gamma_s/\gamma_{us} > 3.5$ for ductile behavior in bcc crystals. To compute the Rice parameters, we use average values of both γ_s and γ_{us}. Figure 4C shows the results, where both γ_s and γ_{us} are calculated with respect to the {110} slip plane, and we verify again that the consideration of the {112} or the {123} slip planes provides the same trends (see fig. S7). We also highlight that the Rice parameter values calculated for NbTaMoW and TaMoReW, shown in Fig. 4C, are in excellent agreement (to within 3%) with prior DFT results presented in (*83*), leading to the same conclusions on ductility trends.

Figure 4C shows that the Rice criterion correlates well with experimentally measured ductility trends. Specifically, we observe that the group IV element concentration appreciably lowers the USF energy (see Fig. 3) resulting in higher γ_s/γ_{us} ratios, satisfying the Rice threshold for ductile behavior in this set of HEAs, consistent with previous atomistic simulations (*22*) for other group IV–enriched bcc HEA compositions. Further, in contrast to the other two criteria discussed above, the Rice criterion correctly classifies MoReW consistent with experimental observations of ductility, as shown in Fig. 4C. Specifically, although MoReW and elemental V, Nb, and Ta do not meet the relation $\gamma_s/\gamma_{us} > 3.5$, the obtained ratios for these materials are appreciably larger than those obtained for the refractory HEAs and elemental Mo and W such that the criterion correctly predicts the overall trends toward increasing ductility through Re additions to Mo-W alloys.

To summarize the results of this subsection, group IV elements and Re additions lead to different effects on the Pugh, Rice-Thomson, and Rice ductility parameters. For both the Pugh and Rice-Thomson parameters, the trends are primarily controlled by the concentration dependence of the shear modulus G, which softens with increasing group IV element concentration, resulting in values corresponding to increased ductility. Re additions, however, do not induce a softening of the alloy's elastic properties, such that MoReW is classified as being brittle according to the Pugh and Rice-Thomson parameters, inconsistent with experimental observations (*8*). By contrast, the compositional trends in the Rice parameter are primarily governed by the USF energy, which is appreciably lowered by both group IV elements and Re additions, leading to predictions of ductility enhancement by both types of elements. In this sense, only the Rice criterion produces trends in ductility behavior of the bcc HEA compositions in line with reported experimental measurements (*5, 6, 8*).

Last, we note that the compositional trends in the ductility parameters considered in this section cannot be reliably assessed on the basis of ROM estimates, i.e., properties derived from composition-weighted averages of those for the pure elements. For example, values of the shear modulus G obtained using the ROM differ by 20 and 75% from direct DFT calculations for NbTaMoW and NbTaTiHf, respectively, which limits the ability of the ROM in providing

reliable Pugh and Rice-Thomson parameters. This large discrepancy found for NbTaTiHf is induced by the elastic instability of the bcc phase in elemental group IV metals. Further, this phase instability challenges the calculations of fully relaxed surface energies for these metals, which values can be only approximated by a constrained ionic optimization (see text S7). ROM-induced uncertainties in the surface energies, combined with important departures from DFT values found in the USF energies (see above), result in ROM-Rice parameter ductility trends that are inconsistent with experimental observations. Specifically, we show in the Supplementary Materials that while some bcc HEAs feature similar ROM-Rice parameters, e.g., 4.27 and 4.20 for HfMoNbTaW and $HfMo_{0.5}NbTaTiZr$, respectively, the experimental compressive fracture strain reported for these materials differs substantially, with respective values of 6% (*84*) and >50% (*85*).

Electronic structure assessment

The results in the prior subsections demonstrate that compositional trends in the screw dislocation core polarization, dislocation vibrational properties, USF energies, and Rice ratio γ_s/γ_{us} all correlate with observed trends in experimental measurements when considering bcc HEAs with and without group IV elements and Re. In this subsection, we consider underlying features of the bulk electronic structure that correlate with these ductility parameters, establishing physically motivated descriptors for intrinsic ductility trends that can be calculated much more efficiently by first-principles methods than dislocation cores or surface and USF energies.

Two characteristic features of d-orbital DOS in elemental bcc transition metals correlate with the structural stability of the bulk bcc lattice: pronounced bimodality and definite bonding/antibonding splitting (*86*), where the former (later) primarily couples with the bcc coordination (*87*) [d-resonance effect (*88*)]. As a result, the DOS of bcc metals and alloys shows a region of (nonzero) low values around the Fermi level, which is referred as the pseudogap (*89*).

We use two descriptors, namely, dip and g_{occ}/g_{bond}, to examine bimodality and the fraction of occupied bonding states in the DOS of the bcc HEAs examined here. To evaluate bimodality, we perform the Hartigan's dip test (*90*). This statistical method measures the distance between the cumulative distribution function of an empirical distribution and the nearest multimodal function (*90*). Briefly, a set of unimodal cumulative distribution functions H_{ij} is generated for all possible intervals $[x_i, x_j]$ of the sample (here, the electronic DOS) cumulative distribution function F. Each H_{ij} is then shifted by a distance d_{ij} to form a band that approximates F, until F is within the band for all range $(-\infty, +\infty)$. Last, the smallest d_{ij} is defined as the dip statistics and is the descriptor in what follows. Systematic assessments (*91*) of the Hartigan's dip test show that this mathematical tool correlates with bimodality as follows

$$\begin{cases} \text{dip} \leq 0.05, \text{substantial bimodality} \\ 0.05 < \text{dip} \leq 0.10, \text{marginal bimodality} \\ \text{dip} \geq 0.10, \text{multimodality} \end{cases} \quad (2)$$

In addition, we highlight that this parameter has been successfully used in previous studies (*92*) to quantify bimodality in the DOS of bcc binary alloys. To assess the fraction of occupied bonding states, we define the descriptor g_{occ}/g_{bond} such that

$$\frac{g_{\text{occ}}}{g_{\text{bond}}} = \frac{\displaystyle\int_{-\infty}^{E_{\text{F}}} n(E)\, dE}{\displaystyle\int_{-\infty}^{E_{\text{pg}}} n(E)\, dE} \qquad (3)$$

where g_{occ} and g_{bond} denote the number of occupied total and bonding states, respectively; $n(E)$ is the electronic DOS; and E_{F} and E_{pg} are the Fermi and pseudogap energy levels, respectively. With this definition, $g_{\text{occ}}/g_{\text{bond}} = 1$ implies that only bonding states are fully occupied, corresponding to maximum structural stability (*93*). Further, $g_{\text{occ}}/g_{\text{bond}} < 1$ or >1 indicate an empty fraction of bonding states or population of antibonding states, respectively, both correlating with a relative destabilization of the bcc lattice. To assess the relevance of the proposed descriptor, we also perform a crystal orbital Hamilton population analysis (*94–96*) to study the filling of bonding states. Results obtained using the crystal orbital Hamilton population method agree qualitatively with those provided by the descriptor $g_{\text{occ}}/g_{\text{bond}}$ and are presented in text S9.

We further assess the nature of dislocation-induced changes in the local DOS (LDOS) near the core. We examine the LDOS projected in the atoms in the first and second nearest-neighbor shells of the screw dislocation core (as labeled in Fig. 1A) corresponding to relaxed bulk and core ground-state configurations (i.e., the 270-atom cell without and with the dislocation dipole, respectively, both structurally optimized). Figure 5 shows the obtained LDOS plots and calculated $g_{\text{occ}}/g_{\text{bond}}$, and Table 1 presents dip descriptors. The core configurations used to calculate the dislocated crystal LDOS are those presented in Fig. 1.

We first focus on the effects of composition on the bulk LDOS, specifically on the fraction of occupied bonding states. As shown in Fig. 5 (A to C), the Fermi level lies close to the pseudogap in the set of refractory (NbTaMo, NbTaMoW, and NbTaMoWV, respectively)
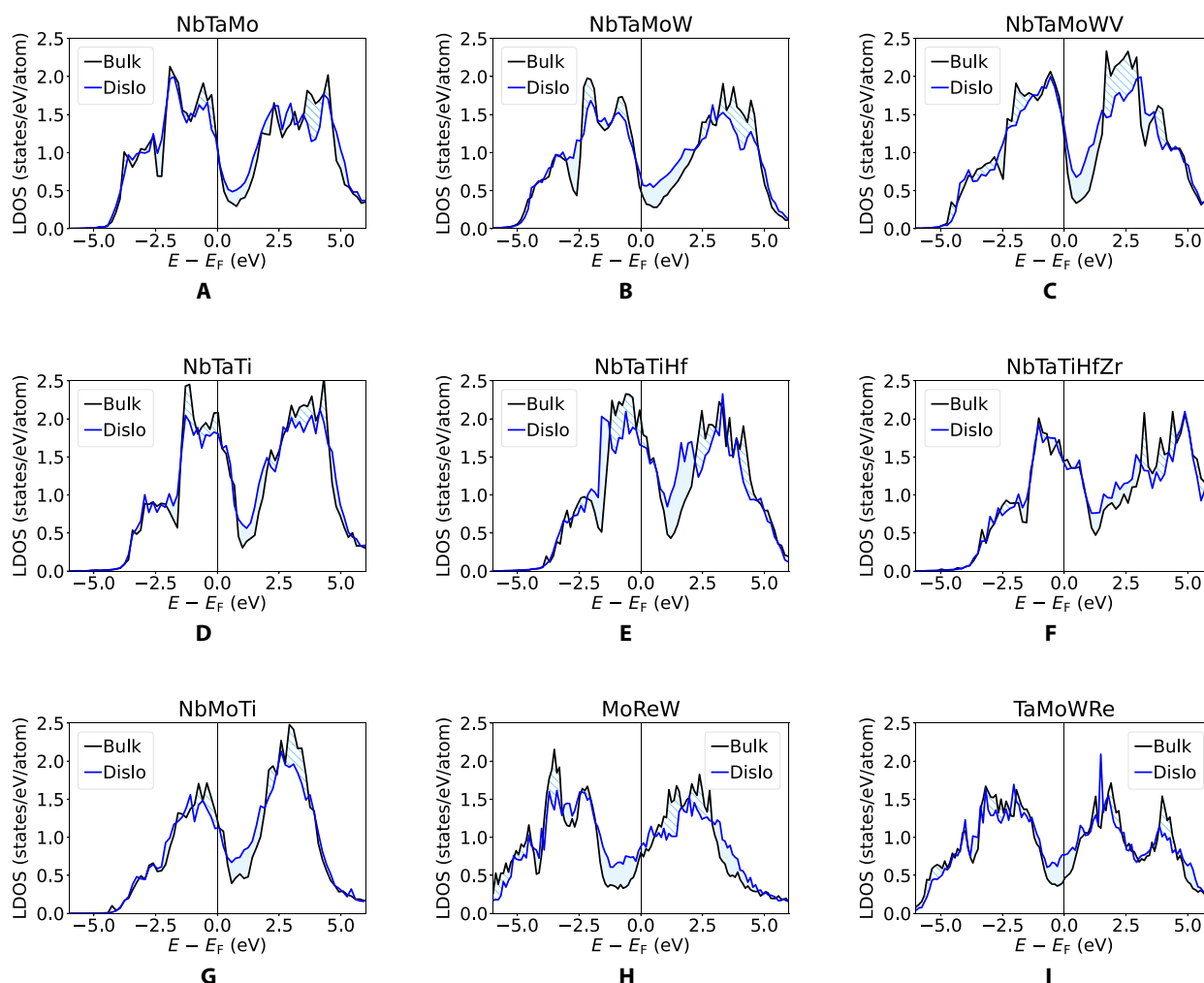

Fig. 5. Local electronic DOS projected onto atoms in bulk and in screw dislocation core configurations. LDOS are plotted for the atoms in the first and second nearest-neighbor shells in relaxed structures corresponding to the bulk (black lines) and dislocation core ground-state (blue lines) configurations obtained in the (**A**) NbTaMo, (**B**) NbTaMoW, (**C**) NbTaMoWV, (**D**) NbTaTi, (**E**) NbTaTiHf, (**F**) NbTaTiHfZr, (**G**) NbMoTi, (**H**) MoReW, and (**I**) TaMoWRe bcc HEAs. The core configurations used to calculate the dislocated crystal LDOS are those shown in Fig. 1. Solid or hatched fillings indicate an enhancement or depletion of the LDOS for the atoms in the dislocation core, respectively, relative to the bulk configuration.

Table 1. Local electronic DOS descriptors. The fraction of occupied bonding states (g_{occ}/g_{bond}) and Hartigan bimodality statistics (dip) calculated for the plots presented in Fig. 5. Relative differences [$\Delta(g_{occ}/g_{bond})$ and Δdip] are computed with respect to the bulk.

	Bulk	Dislocation		Bulk	Dislocation	
	g_{occ}/g_{bond}	g_{occ}/g_{bond}	$\Delta(g_{occ}/g_{bond})$	dip	dip	Δdip
NbTaMo	0.900	0.929	3.2%	0.023	0.029	26.1%
NbTaMoW	0.951	0.950	−0.1%	0.014	0.019	35.7%
NbTaMoWV	0.905	0.936	3.4%	0.025	0.032	28.0%
NbTaTi	0.743	0.737	−0.8%	0.015	0.019	26.7%
NbTaTiHf	0.705	0.722	2.4%	0.014	0.018	28.6%
NbTaTiHfZr	0.686	0.710	3.4%	0.021	0.027	28.5%
MoReW	1.095	1.143	4.4%	0.069	0.095	37.7%
NbMoTi	0.862	0.868	4.6%	0.014	0.019	35.7%
TaMoWRe	1.017	1.080	5.9%	0.041	0.061	48.9%

HEAs resulting in $g_{occ}/g_{bond} \approx 1$. However, in the group IV–containing NbTaTi (Fig. 5D), NbTaTiHf (Fig. 5E), and NbTaTiHfZr (Fig. 5F) HEAs, the Fermi level is shifted toward the bonding states to a degree that is enhanced as the group IV element concentration increases, leading to g_{occ}/g_{bond} ratios appreciably smaller than 1. Further, the Fermi level is located at high values of the LDOS, reflecting an unfavorable structural configuration. By contrast, in MoReW, Fig. 5H shows that the Fermi level is shifted toward the antibonding states such that g_{occ}/g_{bond} is slightly larger than 1.

To complement the g_{occ}/g_{bond} analysis, we also compute the single-crystal elastic moduli (C_{ij}) of the materials considered in this work, which are presented in the Supplementary Materials. We observe that refractory HEAs feature favorable bonding, as shown by the g_{occ}/g_{bond} descriptor and relatively stiffer elastic properties. Despite Re inducing a population of antibonding states, this destabilization effect is mitigated by enlarging the band energy such that bonding remains strong and elastic properties remain stiff in MoReW. In contrast, the group IV element concentration leads to a substantial depletion of occupied bonding states, resulting in a pronounced softening of the elastic moduli, particularly the tetragonal shear modulus (C'), which decreases as the group IV element concentration increases.

Beyond the elastic moduli, bond strength also controls the vibrational spectra. At long wavelengths, acoustic frequencies can be written as a combination of elastic constants (65, 97) such that a softening of C_{ij} correlates with a softening of the vibrational dispersion, both reflecting bond strength softening. This analysis is consistent with the results presented in Fig. 2 and explain the different behavior observed in the NbTaTiHf compared to NbTaMoW and MoReW. In addition, the vibrational dispersion is closely correlated with LLDs (62) as discussed in the "Screw dislocation vibrational properties" section. In this way, bond softening induced by the group IV element concentration also provides insight into the large LLDs observed in the vicinity of dislocation cores in group IV–containing bcc HEAs.

We consider next bimodality. Table 1 shows that, according to the dip statistics, the bulk LDOS of both refractory and group IV–containing bcc HEAs features pronounced bimodality. Despite the large LLD magnitude observed in the NbTaTiHf and NbTaTiHfZr

HEAs leading to a structurally more complex configuration away from the ideal bcc coordination, bimodality is not shown to be importantly affected. However, Re remarkably suppresses bimodality in the MoReW regardless of the low LLDs observed in the bulk. This contrast is visually evident when comparing the NbTaTi LDOS (Fig. 5D) versus those for MoReW (Fig. 5H), where the LDOS close to the Fermi level of the former (latter) shows a narrow (flat) minimum in between two sharp (broad) peaks.

We therefore find that the bulk electronic structure of both group IV–and Re-containing bcc HEAs show features that are destabilizing for the bcc structure but coupled with distinct phenomena. Specifically, the group IV element concentration induces notable bond strength softening while marginally affecting bimodality; conversely, bonding remains strong in the Re-containing HEA while bimodality is appreciably suppressed.

We consider next changes in the LDOS for atoms in the dislocation core versus the bulk. As shown in Fig. 5, the dislocation core induces a pronounced reorganization of the LDOS such that states close to the pseudogap are filled, consistent with results observed in pure bcc metals (43) and binary bcc alloys (92). Quantitatively, Table 1 shows that the dislocation core minimally affects the fraction of occupied bonding states, with g_{occ}/g_{bond} relative changes with respect to the bulk smaller than 5%. Nevertheless, the dislocation core substantially suppresses bimodality as shown by in an increase of approximately 30% of the dip statistics in all bcc HEAs, reflecting the disruption of the bcc coordination in the vicinity of the core as presented in Fig. 1.

We observe that pronounced core asymmetry correlates with incipient structural instabilities observed in the bulk. Specifically, in the structurally stable refractory bcc HEAs, the extent of the structural distortions induced by the dislocation core are relatively localized because of the strong restoring forces in the bulk lattice. However, if the bcc HEA shows incipient structural instabilities (i.e., group IV element or Re concentration), then a longer-range atomic reorganization is observed around the core, resulting in core spreading. Hence, we propose that the screw dislocation core ground-state configuration is an intrinsic material property reflecting details of the electronic structure. Such a dependency on electronic structure likely explain why simple core-controlling criteria based on

thermodynamic properties [e.g., γ-line profile (37)] cannot correctly predict trends of core polarization in complex concentrated alloys (see text S11) (31). In addition, we show in fig. S9 that the characteristic features of the electronic structure are a result of the overall alloy composition and cannot be clearly associated with specific atom types in the core. These results suggest that details of the core structure may not be sensitive to chemical short-range order, consistent with previous computational studies (16, 47).

We consider next correlations between the changes in electronic structure induced by the addition of group IV elements and Re, with the compositional trends in the intrinsic ductility parameters discussed above. The depletion of the fraction of bonding states observed because of the group IV element concentration results in a softening of the material's elastic properties, having important implications for the trends in the Pugh and Rice-Thomson parameters, which shows strong dependence on the shear modulus. Further, a destabilization of the bcc lattice, reflected by either bond softening or bimodality suppression, arising from group IV elements or Re additions, respectively, is correlated with a lowering of the USF energy. This property strongly affects the trends in the Rice parameter such that a destabilization of the bcc lattice accompanies improvements in ductility predicted by this parameter, consistent with experimental observations across the bcc HEA compositions (5, 6, 8).

The present study outlines features of the alloy's bulk electronic structure that correlate with structural stability, degree of screw dislocation core polarization, USF energy, and measurements of intrinsic ductility reflected by the Rice criterion. Further, compositional variations for all of these properties are shown to correlate with reported trends in experimental observations for ductility across bcc HEA considered. Hence, characteristics of the electronic structure, i.e., the fraction of occupied bonding states and bimodality, can be used to gauge the potential for intrinsic ductility in bcc HEAs. To further verify the consistency of our proposed descriptors in capturing experimental observations, we include in our analyses NbMoTi and TaMoWRe, which, despite being respectively group IV element–and Re-containing bcc HEAs, have been reported to show brittle behavior at room temperature (7, 13). LDOS plots and calculated electronic descriptors for these materials are presented alongside other alloy compositions in Fig. 5 and Table 1, and screw dislocation core properties and unstable stacking energy values are presented in the Supplementary Materials.

The bulk electronic structure of both NbMoTi and TaMoWRe shows destabilizing features for the bcc structure, respectively, depletion of the fraction of occupied bonding states and suppression of bimodality, but not as substantial as other group IV element–and Re-containing compositions considered above. As a result, the screw dislocation core ground-state configuration in NbMoTi and TaMoWRe shows less pronounced polarization (see table S2).

A more important contrast between the properties of NbMoTi and TaMoWRe and other studied HEA compositions is observed in the USF energy values. Specifically regarding TaMoWRe, the Re concentration is not enough to lower γ_{us} values such that this alloy shows the highest USF energies among all considered HEAs (see table S4), resulting in poor intrinsic ductility reflected by the Rice parameter (see Fig. 4C). In the case of NbMoTi, whereas the Ti concentration induces isotropy between high-order planes as the difference between γ_{us} values along {110} and {123} is close to 6%, the USF energy magnitudes remain appreciably high, also leading to intrinsic brittle behavior according to the Rice ratio (see Fig. 4C).

Our DFT calculations for NbMoTi are fully consistent with experimental observations: While the ternary alloy shows active screw dislocation slip along high-order planes (27), correlating with USF energy isotropy, the material also shows tensile brittle behavior (13), in agreement with the Rice parameter.

DISCUSSION

The present DFT calculations demonstrate that alloy chemistry can be tuned to profoundly alter dislocation slip behavior and intrinsic ductility in bcc HEAs. Specifically, the results indicate that additions of group IV elements and Re to alloys based solely on (groups V and VI) bcc elements promote screw dislocation core polarization and lowering of USF energy values. A consequence of this synergy of chemically induced changes in material properties is reflected in improvements in intrinsic ductility measured by the Rice parameter.

Further, the intrinsic ductility trends are linked to key characteristics of the electronic DOS, namely, the fraction of occupied bonding states and bimodality. Group IV elements and Re additions induce bonding softening and bimodality suppression, respectively, both representing features of the electronic DOS that are destabilizing for the bcc structure in transition-metal alloys. This destabilization is shown to be closely correlated to screw dislocation core spreading and USF energy lowering.

Hence, we propose that the fraction of occupied bonding states (g_{occ}/g_{bond}) and bimodality (dip) descriptors calculated for the bulk configuration can be used to assess the potential for intrinsic ductility in bcc HEAs. To further test this approach, g_{occ}/g_{bond} and dip electronic descriptors are calculated for more than 50 bcc complex concentrated alloys, from binaries to six-element materials, including nonequiatomic compositions (see table S6). In these DOS calculations, cubic 54-atom bulk cells are used (see texts S12 and S13). To enable correlation of these results with experimental compressive fracture strains (ε_p), the 50 additional compositions are chosen for alloys where these experimental values have been reported in the literature (see table S6).

As illustrated in Fig. 6A, we find that the descriptors allow to distinguish the compositions in two major groups, one of which is controlled by incomplete filling of bonding states and other by bimodality suppression. In detail, Fig. 6B shows that bcc alloys showing substantial depletion of bonding states ($g_{occ}/g_{bond} < 0.8$) feature high intrinsic ductility, correlating with experimental observations of $\varepsilon_p > 30\%$. Conversely, compositions showing bonding states almost completely filled ($0.9 < g_{occ}/g_{bond} < 1.0$) are brittle, correlating with $\varepsilon_p < 5\%$. We further observe that, for intermediate degrees of bonding filling ($0.8 < g_{occ}/g_{bond} < 0.9$), g_{occ}/g_{bond} correlates monotonically with ε_p, suggesting that g_{occ}/g_{bond} is able not only to classify but also to satisfactorily rank the potential for intrinsic ductility across bcc complex concentrated alloy compositions. In addition, Fig. 6B shows that compositions featuring all bonding states occupied ($g_{occ}/g_{bond} > 1$) have intrinsic ductility controlled by bimodality suppression, showing ductile behavior in experimental measurements only if dip > 0.05.

The descriptors g_{occ}/g_{bond} and dip thus can be used to assess ductility trends consistent with experimental measurements from compression tests. Use of these descriptors thus provides a strategy for screening alloy compositions that improves on approaches based on average valence electron count or ROM approaches, as discussed in the Supplementary Materials.
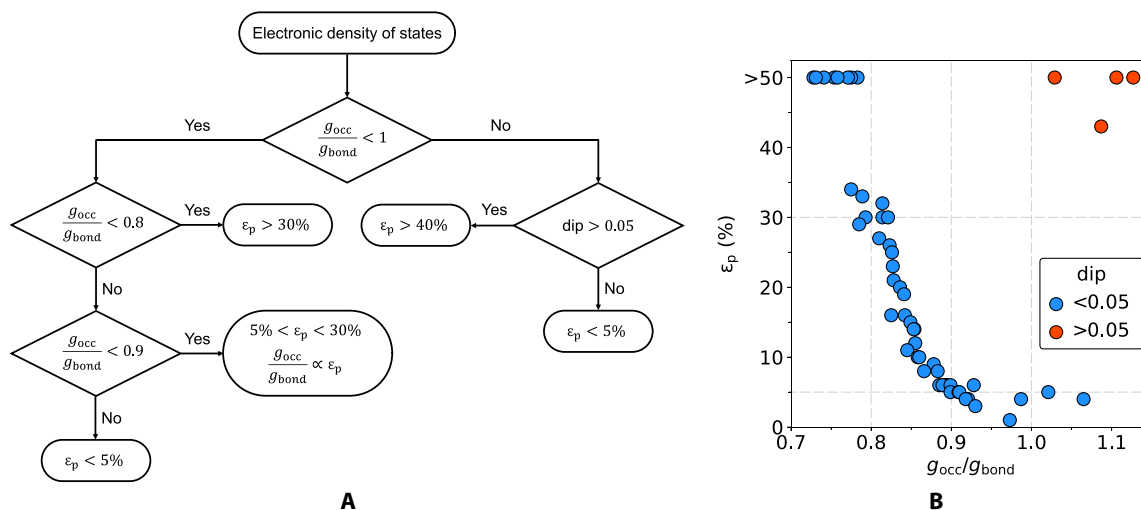
Fig. 6. Electronic intrinsic ductility assessment. (**A**) Flow chart for intrinsic ductility assessment using the fraction of bonding states (g_{occ}/g_{bond}) and bimodality (dip) electronic descriptors. (**B**) Correlations between g_{occ}/g_{bond} and dip with experimental compressive fracture strains (ε_p) reported in the literature (see table S6) for bcc complex concentrated alloys.

We emphasize that g_{occ}/g_{bond} and dip values shown in Fig. 6B are calculated using cubic 54-atom bulk cells, not requiring the calculation of defect properties within large cell geometries (~250 atoms). DFT calculations scale in general with the cube of the number of atoms; if computer budget is dominated by the operations that lead to this scaling, then less than 2% of the resources required by the large cells would be required for the smaller 54-atom cells. On the basis of our experience, this relation is consistent with the time required to relax these cell geometries in our DFT calculations. We find that the total computational expense to calculate the descriptors for all compositions shown in Fig. 6B is smaller than that for calculating the Rice parameter (i.e., surface and USF energies) for a single bcc HEA.

In summary, this work correlates key signatures in the electronic structure of bcc HEAs to dislocation deformation behavior and intrinsic ductility. We propose that the values of the fraction of occupied bonding states lower than 0.8 or bimodality values greater than 0.05 in the bulk electronic DOS provide a basis for screening for high intrinsic ductility in computationally accelerated design of bcc HEAs composed of transition-metal elements.

MATERIALS AND METHODS
First-principles calculations
All first-principles calculations reported in this work are performed within DFT as implemented in the Vienna ab initio simulation package code (*98–100*). The projector augmented wave formalism (*101*, *102*) is used with the Perdew-Burke-Ernzerhof generalized gradient approximation (*103*) to model the exchange-correlation potential. A plane-wave basis set with a kinetic energy cutoff of 600 eV is used, and in the *k*-point sampling, we use the Methfessel-Paxton scheme (*104*) with a smearing of 0.2 eV. The projector augmented wave potentials used treat 10, 12, 10, 11, 11, 11, 12, 12, and 13 electrons as valence for Ti, Zr, Hf, V, Nb, Ta, Mo, W and Re, respectively (i.e., we include semicore states for all elements). Atomic relaxation is carried out with the conjugate gradient method in simulation cells with fixed periodic vectors (i.e., at constant cell shape

and volume) at the equilibrium lattice parameter, until residual forces have magnitudes below a tolerance of 5 meV/Å. We use a different tolerance criterion for the USF energy calculations (see below).

The electronic DOS plots are calculated for relaxed structures using the tetrahedron method with Blöchl corrections (*105*) to perform Brillouin-zone integrations. All other DFT parameters are the same as those presented above, and we use the same *k*-point grid used for structural relaxation of screw dislocation cores (see below).

Atomic vibrations are calculated at the harmonic level using the finite difference approach, as implemented in the Phonopy package (*106*). The vibrational spectra are computed using the full force-constant matrix for both the bulk and the dislocation dipole configurations and thus sample the mass and force-constant fluctuations present in these systems. We use an energy converge tolerance of <10^{-7} eV for the electron self-consistency criterion in these calculations and use the same *k*-point grid used for structural relaxation of screw dislocation cores (see below). The VDOS presented in this manuscript is derived from dislocation supercells that are relatively thin in the ⟨111⟩ direction (i.e., the dislocation line direction). To check the convergence of the results obtained using these supercell geometries, we compare results for bulk VDOS to those derived from cubic 54-atom supercells. The latter have been shown to provide well-converged vibrational properties of bcc HEAs in (*66*, *67*). The frequency gravity center of the total bulk VDOS calculated by the dislocation and cubic supercells agree to within 2% for the bcc HEA compositions shown in Fig. 2. We also find that the presently calculated frequency gravity center of the total bulk VDOS for NbToMoW agrees within 1% of the value reported in (*67*).

Simulation cell
Chemical disorder in the bcc HEAs is modeled using the SQS approach (*32*). We use the Monte Carlo Special Quasirandom Structure (MCSQS) (*107*) package in the Alloy Theoretic Automated Toolkit to generate the SQS models, which are constructed to provide correlation functions for the first two neighbor shells that approximate a random solution for all constituent elements.

$1/2 \langle 111 \rangle$ screw dislocations are modeled using a quadrupolar arrangement with triperiodic boundary conditions (*108, 109*). The simulation cell periodicity vectors $\{\mathbf{p}_1, \mathbf{p}_2, \mathbf{p}_3\}$ are as follows: $\mathbf{p}_1 = 5/2\ \mathbf{u}_1 - 9/2\ \mathbf{u}_2$, $\mathbf{p}_2 = 5/2\ \mathbf{u}_1 + 9/2\ \mathbf{u}_2$, and $\mathbf{p}_3 = 2\ \mathbf{u}_3$, where $\mathbf{u}_1 = a_0[1\bar{1}2]$, $\mathbf{u}_2 = a_0[1\bar{1}0]$, and $\mathbf{u}_3 = a_0/2\ [111]$ are the elementary vectors. The simulation cell has twice the magnitude of the Burgers vector along the dislocation line direction parallel to $\mathbf{p}_3$, containing a total of 270 atoms. We highlight that such a supercell geometry has been shown to provide well-converged core structures in elemental bcc metals in previous DFT studies (*43, 44*). A dislocation dipole of Burgers vector $\vec{b} = -a_0/2\ [111]$ is introduced in the simulation cell using anisotropic elasticity theory as implemented in the Babel package (*110*). To sample the Brillouin zone in the DFT dislocation calculations, we make use of a Γ-centered $2 \times 2 \times 8$ k-point grid. For each HEA composition, we examine five different SQS models to compute core polarization parameters.

Surface (γ_s) and USF (γ_{us}) energies along the (i) {110}, (ii) {112}, and (iii) {123} slip planes are calculated using orthogonal cells with axes: (i) $2a_0\ [1\bar{1}2] \times 6a_0\ [1\bar{1}0] + \Delta \times 2a_0\ [111]$, (ii) $3a_0\ [1\bar{1}0] \times 4a_0\ [1\bar{1}2] + \Delta \times 2a_0\ [111]$, and (iii) $a_0\ [5\bar{4}1] \times 2a_0\ [12\bar{3}] + \Delta \times 3a_0/2\ [111]$, where Δ is a 15-Å vacuum gap. These configurations lead to cells containing a total of (i) 288, (ii) 288, and (iii) 252 atoms, corresponding to (i) 12, (ii) 24, and (iii) 28 atomic layers along the y direction. These supercell geometries have similar number of layers along the y direction to those used in previous DFT studies (*111, 112*); to obtain the configurations described above, we further replicate the reference geometry along x and z directions to sample fluctuations associated with the compositional disorder. Surface energies are obtained allowing a full relaxation of all Cartesian coordinates and are computed using the expression: $\gamma_s = (E_{slab} - E_{bulk})/(2A_{slab})$, where E_{slab} and E_{bulk} are the energies of cell with and without the vacuum gap, respectively, and A_{slab} is the slab surface area in the xz plane. To obtain the USF energies, the top half layers are displaced by $\vec{b}/2$ with respect to the bottom half layers, where $\vec{b}$ is the Burgers vector defined above. A constrained ionic relaxation is performed such that the N_{fix}-top and N_{fix}-bottom layers are fixed, with N_{fix} equals to (i) 2, (ii) 3, and (iii) 4, and atoms in the middle layers are allowed to relax only along the y direction. The relaxation is carried out until the total energy difference between two consecutive ionic steps is smaller than 10^{-6} eV. USF energies are then calculated using $\gamma_{us} = (E_{us} - E_s)/A_{slab}$, where E_{us} and E_s are the energies of the displaced and nondisplaced cells, respectively. In these DFT calculations, we use a Γ-centered $8 \times 2 \times 4$ k-point grid to sample the Brillouin zone. We compute γ_s and γ_{us} energy values for three different SQS models for each HEA composition and slip plane.

Supplementary Materials

This PDF file includes:
Supplementary Text S1 to S14
Figs. S1 to S12
Tables S1 to S6
References

REFERENCES AND NOTES

1. D. B. Miracle, O. N. Senkov, A critical review of high entropy alloys and related concepts. *Acta Mater.* **122**, 448–511 (2017).
2. E. P. George, D. Raabe, R. O. Ritchie, High-entropy alloys. *Nat. Rev. Mater.* **4**, 515–534 (2019).
3. O. N. Senkov, D. B. Miracle, K. J. Chaput, J.-P. Couzinie, Development and exploration of refractory high entropy alloys–a review. *J. Mater. Res.* **33**, 3092–3128 (2018).
4. O. N. Senkov, G. B. Wilks, D. B. Miracle, C. P. Chuang, P. K. Liaw, Refractory high-entropy alloys. *Intermetallics* **18**, 1758–1765 (2010).
5. O. N. Senkov, G. B. Wilks, J. M. Scott, D. B. Miracle, Mechanical properties of Nb25Mo25Ta25W25 and V20Nb20Mo20Ta20W20 refractory high entropy alloys. *Intermetallics* **19**, 698–706 (2011).
6. O. N. Senkov, J. M. Scott, S. V. Senkova, D. B. Miracle, C. F. Woodward, Microstructure and room temperature properties of a high-entropy TaNbHfZrTi alloy. *J. Alloys Compd.* **509**, 6043–6048 (2011).
7. Y. Wan, Q. Wang, J. Mo, Z. Zhang, X. Wang, X. Liang, B. Shen, WReTaMo refractory high-entropy alloy with high strength at 1600°C. *Adv. Eng. Mater.* **24**, 202100765 (2022).
8. O. N. Senkov, S. I. Rao, G. H. Balbus, R. Wheeler, E. J. Payton, Microstructure and deformation behavior of MoReW in the temperature range from 25°C to 1500°C. *Materialia* **27**, 101688 (2023).
9. X. J. Fan, R. T. Qu, Z. F. Zhang, Remarkably high fracture toughness of HfNbTaTiZr refractory high-entropy alloy. *J. Mater. Sci. Technol.* **123**, 70–77 (2022).
10. D. H. Cook, P. Kumar, M. I. Payne, C. H. Belcher, P. Borges, W. Wang, F. Walsh, Z. Li, A. Devaraj, M. Zhang, M. Asta, A. M. Minor, E. J. Lavernia, D. Apelian, R. O. Ritchie, Kink bands promote exceptional fracture resistance in a NbTaTiHf refractory medium-entropy alloy. *Science* **384**, 178–184 (2024).
11. S. Wang, M. Wu, D. Shu, G. Zhu, D. Wang, B. Sun, Mechanical instability and tensile properties of TiZrHfNbTa high entropy alloy at cryogenic temperatures. *Acta Mater.* **201**, 517–527 (2020).
12. X. Wen, L. Zhu, M. Naeem, H. Huang, S. Jiang, H. Wang, X. Liu, X. Zhang, X.-L. Wang, Y. Wu, Z. Lu, Strong work-hardenable body-centered-cubic high-entropy alloys at cryogenic temperature. *Scr. Mater.* **231**, 115434 (2023).
13. F. Wang, G. H. Balbus, S. Xu, Y. Su, J. Shin, P. F. Rottmann, K. E. Knipling, J.-C. Stinville, L. H. Mills, O. N. Senkov, I. J. Beyerlein, T. M. Pollock, D. S. Gianola, Multiplicity of dislocation pathways in a refractory multiprincipal element alloy. *Science* **370**, 95–101 (2020).
14. S. Wang, M. Wu, D. Shu, B. Sun, Kinking in a refractory TiZrHfNb0.7 medium-entropy alloy. *Mater. Lett.* **264**, 127369 (2020).
15. X. Zhou, X. Wang, L. Fey, S. He, I. Beyerlein, P. Cao, J. Marian, Models of dislocation glide and strengthening mechanisms in bcc complex concentrated alloys. *MRS Bull.* **48**, 777–789 (2023).
16. S. Yin, J. Ding, M. Asta, R. O. Ritchie, Ab initio modeling of the energy landscape for screw dislocations in body-centered cubic high-entropy alloys. *npj Comput. Mater.* **6**, 110 (2020).
17. I. Toda-Caraballo, P. E. J. Rivera-Diaz-del-Castillo, Modelling solid solution hardening in high entropy alloys. *Acta Mater.* **85**, 14–23 (2015).
18. C. Lee, G. Song, M. C. Gao, R. Feng, P. Chen, J. Brechtl, Y. Chen, K. An, W. Guo, J. D. Poplawsky, S. Li, A. T. Samaei, W. Chen, A. Hu, H. Choo, P. K. Liaw, Lattice distortion in a strong and ductile refractory high-entropy alloy. *Acta Mater.* **160**, 158–172 (2018).
19. S. I. Rao, B. Akdim, E. Antillon, C. Woodward, T. A. Parthasarathy, O. N. Senkov, Modeling solution hardening in BCC refractory complex concentrated alloys: NbTiZr, Nb1.5TiZr0.5 and Nb0.5TiZr1.5. *Acta Mater.* **168**, 222–236 (2019).
20. C. Baruffi, F. Maresca, W. A. Curtin, Screw vs. edge dislocation strengthening in body-centered-cubic high entropy alloys and implications for guided alloy design. *MRS Commun.* **12**, 1111–1118 (2022).
21. O. N. Senkov, D. B. Miracle, S. I. Rao, Correlations to improve room temperature ductility of refractory complex concentrated alloys. *Mater. Sci. Eng. A* **820**, 141512 (2021).
22. E. Mak, B. Yin, W. A. Curtin, A ductility criterion for bcc high entropy alloys. *J. Mech. Phys. Solids* **152**, 104389 (2021).
23. P. Singh, B. Vela, G. Ouyang, N. Argibay, J. Cui, R. Arroyave, D. D. Johnson, A ductility metric for refractory-based multi-principal-element alloys. *Acta Mater.* **257**, 119104 (2023).
24. J.-P. Couzinie, L. Lilensten, Y. Champion, G. Dirras, L. Perriere, I. Guillot, On the room temperature deformation mechanisms of a TiZrHfNbTa refractory high-entropy alloy. *Mater. Sci. Eng. A* **645**, 255–263 (2015).
25. H. Y. Yasuda, Y. Yamada, K. Cho, T. Nagase, Deformation behavior of HfNbTaTiZr high entropy alloy singe crystals and polycrystals. *Mater. Sci. Eng. A* **809**, 140983 (2021).
26. Y. Bu, Y. Wu, Z. Lei, X. Yuan, H. Wu, X. Feng, J. Liu, J. Ding, Y. Lu, H. Wang, Z. Lu, W. Yang, Local chemical fluctuation mediated ductility in body-centered-cubic high-entropy alloys. *Mater. Today* **46**, 28–34 (2021).
27. G. H. Balbus, S. I. Rao, O. N. Senkov, E. J. Payton, Orientation dependent plasticity of the refractory multi-principal element alloy MoNbTi investigated via micropillar compression. *Acta Mater.* **262**, 119401 (2023).
28. T. Tsuru, S. Han, S. Matsuura, Z. Chen, K. Kishida, I. Iobzenko, S. I. Rao, C. Woodward, E. P. George, H. Inui, Intrinsic factors responsible for brittle versus ductile nature of refractory high-entropy alloys. *Nat. Commun.* **15**, 1706 (2024).
29. T. Leveau, L. Ventelon, E. Clouet, Interaction of C, N and O interstitial solute atoms with screw dislocations in HfNbTaTiZr high entropy alloy. *Acta Mater.* **275**, 120062 (2024).
30. J. P. Hirth, J. Lothe, *Theory of Dislocations* (Wiley, 1982).

31. L. Romaner, C. Ambrosch-Draxl, R. Pippan, Effect of rhenium on the dislocation core structure in tungsten. *Phys. Rev. Lett.* **104**, 195503 (2010).

32. A. Zunger, S.-H. Wei, L. G. Ferreira, J. E. Bernard, Special quasirandom structures. *Phys. Rev. Lett.* **65**, 353–356 (1990).

33. S. F. Pugh, Relations between the elastic moduli and the plastic properties of polycrystalline pure metals. *Philos. Mag.* **45**, 823–843 (1954).

34. J. R. Rice, R. Thomson, Ductile versus brittle behaviour of crystals. *Philos. Mag.* **29**, 73–97 (1974).

35. J. R. Rice, Dislocation nucleation from a crack tip: An analysis based on the Peierls concept. *J. Mech. Phys. Solids* **40**, 239–271 (1992).

36. V. Vitek, Theory of the core structures of dislocations in body-centred-cubic metals. *Cryst. Latt. Def.* **5**, 1–34 (1974).

37. M. S. Duesbery, V. Vitek, Plastic anisotropy in b.c.c. transition metals. *Acta Mater.* **46**, 1481–1492 (1998).

38. C. Woodward, S. I. Rao, Ab-initio simulation of isolated screw dislocations in bcc Mo and Ta. *Philos. Mag. A* **81**, 1305–1316 (2001).

39. G. Wang, A. Strachan, T. Cagin, W. A. Goddard, Role of core polarization curvature of screw dislocations in determining the Peierls stress in bcc Ta: A criterion for designing high-performance materials. *Phys. Rev. B* **67**, 140101 (2003).

40. S. Ismail-Beigi, T. A. Arias, Ab initio study of screw dislocations in Mo and Ta: A new picture of plasticity in bcc transition metals. *Phys. Rev. Lett.* **84**, 1499–1502 (2000).

41. C. Woodward, S. I. Rao, Flexible ab initio boundary conditions: Simulating isolated dislocations in bcc Mo and Ta. *Phys. Rev. Lett.* **88**, 216402 (2002).

42. L. Ventelon, F. Willaime, Core structure and Peierls potential of screw dislocations in α-Fe from first principles: Cluster versus dipole approaches. *J. Comput. Aided Mol. Des.* **14**, 85–94 (2007).

43. L. Dezerald, L. Ventelon, E. Clouet, C. Denoual, D. Rodney, F. Willaime, Ab initio modeling of the two-dimensional energy landscape of screw dislocations in bcc transition metals. *Phys. Rev. B* **89**, 024104 (2014).

44. E. Clouet, B. Bienvenu, L. Dezerald, D. Rodney, Screw dislocations in BCC transition metals: From ab initio modeling to yield criterion. *C. R. Phys.* **22**, 83–116 (2021).

45. L. Ventelon, F. Willaime, Generalized stacking-faults and screw-dislocation core-structure in bcc iron: A comparison between ab initio calculations and empirical potentials. *Philos. Mag.* **90**, 1063–1074 (2010).

46. C. Hartley, Y. Mishin, Characterization and visualization of the lattice misfit associated with dislocation cores. *Acta Mater.* **53**, 1313–1321 (2005).

47. W. Wang, F. Walsh, R. O. Ritchie, M. Asta, Elucidating the roles of chemistry, compositional complexity, and short-range order in the dislocation energetics of body-centered-cubic concentrated solid solutions. *Phys. Rev. Mater.* **8**, 013608 (2024).

48. B. Akdim, C. Woodward, S. Rao, E. Antillon, Predicting core structure variations and spontaneous partial kink formation for 1/2<111> screw dislocations in three BCC NbTiZr alloys. *Scr. Mater.* **199**, 113834 (2021).

49. H. Li, S. Wurster, C. Motz, L. Romaner, C. Ambrosch-Draxl, R. Pippan, Dislocation-core symmetry and slip planes in tungsten alloys: Ab initio calculations and microcantilever bending experiments. *Acta Mater.* **60**, 748–758 (2012).

50. L. Dezerald, D. Rodney, E. Clouet, L. Ventelon, F. Willaime, Plastic anisotropy and dislocation trajectory in BCC metals. *Nat. Commun.* **7**, 11695 (2016).

51. H. Chen, T. Hanemann, S. Seils, D. Schliephake, A. S. Tirunilai, M. Heilmaier, K.-P. Weiss, A. Kauffmann, Influence of temperature and plastic strain on deformation mechanisms and kink band formation in homogenized HfNbTaTiZr. *Crystals* **11**, 81 (2021).

52. S. Wang, S. Lu, M. Wu, D. Wang, G. Zhu, C. Yang, D. Shu, B. Sun, L. Vitos, Decreasing Zr content to improve tensile properties of non-equiatomic TiZrHfNb medium entropy alloys with transformation-induced plasticity. *Mater. Sci. Eng. A* **832**, 142476 (2022).

53. M. A. Charpagne, J. C. Stinville, F. Wang, N. Philips, T. M. Pollock, Orientation dependent plastic localization in the refractory high entropy alloy HfNbTaTiZr at room temperature. *Mater. Sci. Eng. A* **848**, 143291 (2022).

54. B. Wang, X. Shan, H. Zhao, S. Bai, B. Wang, Y. Tian, Y. Tang, High-temperature deformation behavior and microstructural evolution of NbZrTiTa refractory high entropy alloy. *J. Alloys Compd.* **936**, 168059 (2023).

55. O. N. Senkov, J. Gild, T. M. Butler, Microstructure, mechanical properties and oxidation behavior of NbTaTi and NbTaZr refractory alloys. *J. Alloys Compd.* **862**, 158003 (2021).

56. Q. Li, H. Zhang, D. Li, Z. Chen, S. Huang, Z. Lu, H. Yan, W$_x$NbMoTa refractory high-entropy alloys fabricated by laser cladding deposition. *Materials* **12**, 533 (2019).

57. Z. Sun, K. Xiong, C. Jin, S. Zhang, L. Guo, H. Wu, J. He, L. Wu, K. Wang, Y. Wang, Y. Mao, An experimental and computational design low-modulus (HfNbTa)$_{1-x}$Ti$_x$ multiprinciple elemental alloys with super formability for biomedical applications. *Mater. Sci. Eng. A* **876**, 145137 (2023).

58. J. R. Stephens, Dislocation structures in single-crystal tungsten and tungsten alloys. *Metall. Trans.* **1**, 1293–1301 (1970).

59. M. Garfinkle, *Room-Temperature Tensile Behavior of ⟨100⟩ Oriented Tungsten Single Crystals with Rhenium in Dilute Solid Solution* (NASA Lewis Research Center, 1977).

60. E. Clouet, L. Ventelon, F. Willaime, Dislocation core energies and core fields from first principles. *Phys. Rev. Lett.* **102**, 055502 (2009).

61. Y. Ikeda, K. Gubaev, J. Neugebauer, B. Grabowski, F. Kormann, Chemically induced local lattice distortions versus structural phase transformations in compositionally complex alloys. *npj Comput. Mater.* **7**, 34 (2021).

62. P. P. P. O. Borges, R. O. Ritchie, M. Asta, Local lattice distortions and the structural instabilities in bcc Nb-Ta-Ti-Hf high-entropy alloys: An ab initio computational study. *Acta Mater.* **262**, 119415 (2024).

63. B. Chen, S. Li, J. Ding, X. Ding, J. Sun, E. Ma, Correlating dislocation mobility with local lattice distortion in refractory multi-principal element alloys. *Scr. Mater.* **222**, 115048 (2023).

64. M. S. Nitol, M. J. Echeverria, K. Dang, M. I. Baskes, S. J. Fensin, New modified embedded-atom method interatomic potential to understand deformation behavior in VNbTaTiZr refractory high entropy alloy. *Comput. Mater. Sci.* **237**, 112886 (2024).

65. N. W. Ashcroft, N. D. Mermin, *Solid State Physics* (Saunders College, 1976).

66. Y. Ikeda, A. Carreras, A. Seko, A. Togo, I. Tanaka, Mode decomposition based on crystallographic symmetry in the band-unfolding method. *Phys. Rev. B* **95**, 024305 (2017).

67. F. Kormann, Y. Ikeda, B. Grabowski, M. H. F. Sluiter, Phonon broadening in high entropy alloys. *npj Comput. Mater.* **3**, 36 (2017).

68. G. D. Samolyuk, Y. N. Osetsky, G. M. Stocks, J. R. Morris, Role of static displacements in stabilizing body centered cubic high entropy alloys. *Phys. Rev. Lett.* **126**, 025501 (2021).

69. P. Carruthers, Theory of thermal conductivity of solids at low temperatures. *Peter Carruthers. Rev. Mod. Phys.* **33**, 92–138 (1961).

70. T. Ninomiya, Frictional force on a dislocation–Fluttering mechanism. *Scr. Metall.* **18**, 669–672 (1984).

71. T. Ninomiya, Dislocation vibration and phonon scattering. *J. Physical Soc. Japan* **25**, 830–840 (1968).

72. J. D. Eshelby, The interaction of kinks and elastic waves. *Proc. R. Soc. Lond. A Math. Phys. Sci.* **266**, 222–246 (1962).

73. F. Maresca, W. A. Curtin, Theory of screw dislocation strengthening in random BCC alloys from dilute to "high-entropy" alloys. *Acta Mater.* **182**, 144–162 (2020).

74. B. Joos, M. S. Duesbery, The Peierls stress of dislocations: An analytic formula. *Phys. Rev. Lett.* **78**, 266–269 (1997).

75. A. H. W. Ngan, A generalized Peierls-Nabarro model for nonplanar screw dislocation cores. *J. Mech. Phys. Solids* **45**, 903–921 (1997).

76. J. Huang, H. Xing, J. Sun, Structural stability and generalized stacking fault energies in β Ti–Nb alloys: Relation to dislocation properties. *Scr. Mater.* **66**, 682–685 (2012).

77. X. Wang, S. Xu, W.-R. Jian, X.-G. Li, Y. Su, I. J. Beyerlein, Generalized stacking fault energies and Peierls stresses in refractory body-centered cubic metals from machine learning-based interatomic potentials. *Comput. Mater. Sci.* **192**, 110364 (2021).

78. L. Dezerald, L. Proville, L. Ventelon, F. Willaime, D. Rodney, First-principles prediction of kink-pair activation enthalpy on screw dislocations in bcc transition metals: V, Nb, Ta, Mo, W, and Fe. *Phys. Rev. B* **91**, 094105 (2015).

79. Y. Tong, S. Zhao, H. Bei, T. Egami, Y. Zhang, F. Zhang, Severe local lattice distortion in Zr- and/or Hf-containing refractory multi-principal element alloys. *Acta Mater.* **183**, 172–181 (2020).

80. L. Qi, D. C. Chrzan, Tuning ideal tensile strengths and intrinsic ductility of bcc refractory alloys. *Phys. Rev. Lett.* **112**, 115503 (2014).

81. R. Hill, The elastic behaviour of a crystalline aggregate. *Proc. Phys. Soc. A* **65**, 349–354 (1952).

82. H. Niu, X.-Q. Chen, P. Liu, W. Xing, X. Cheng, D. Li, Y. Li, Extra-electron induced covalent strengthening and generalization of intrinsic ductile-to-brittle criterion. *Sci. Rep.* **2**, 718 (2012).

83. Y.-J. Hu, A. Sundar, S. Ogata, L. Qi, Screening of generalized stacking fault energies, surface energies and intrinsic ductile potency of refractory multicomponent alloys. *Acta Mater.* **210**, 116800 (2021).

84. Y. Tong, L. Bai, X. Liang, Y. Chen, Z. Zhang, J. Liu, Y. Li, Y. Hu, Influence of alloying elements on mechanical and electronic properties of NbMoTaWX (X = Cr, Zr, V, Hf and Re) refractory high entropy alloys. *Intermetallics* **126**, 106928 (2020).

85. C.-C. Juan, K.-K. Tseng, W.-L. Hsu, M.-H. Tsai, C.-W. Tsai, C.-M. Lin, S.-K. Chen, S.-J. Lin, J.-W. Yeh, Solution strengthening of ductile refractory HfMo$_x$NbTaTiZr high-entropy alloys. *Mater. Lett.* **175**, 284–287 (2016).

86. D. G. Pettifor, *Bonding and Structure of Molecules and Solids* (Clarendon Press, 1995).

87. B. Seiser, T. Hammerschmidt, A. N. Kolmogorov, R. Drautz, D. G. Pettifor, Theory of structural trends within 4*d* and 5*d* transition metal topologically close-packed phases. *Phys. Rev. B* **83**, 224116 (2011).

88. P. Ravindran, R. Asokamani, Correlation between electronic structure, mechanical properties and phase stability in intermetallic compounds. *Bull. Mater. Sci.* **20**, 613–622 (1997).

89. O. Gourdon, D. Gout, G. J. Miller, Electronic states of intermetallic compounds, in *Encyclopedia of Condensed Matter Physics*, F. Bassani, G. L. Liedl, P. Wyder, Eds. (Elsevier, Oxford, 2005), pp. 409–422.

90. J. A. Hartigan, P. M. Hartigan, The dip test of unimodality. *Ann. Stat.* **13**, 70–84 (1985).

91. J. B. Freeman, R. Dale, Assessing bimodality to detect the presence of a dual cognitive process. *Behav. Res. Methods* **45**, 83–97 (2012).

92. Y.-J. Hu, G. Zhao, B. Zhang, C. Yang, M. Zhang, Z.-K. Liu, X. Qian, L. Qi, Local electronic descriptors for solute-defect interactions in bcc refractory metals. *Nat. Commun.* **10**, 4484 (2019).

93. J.-H. Xu, A. J. Freeman, Band filling and structural stability of cubic trialuminides: YAl₃, ZrAl₃, and NbAl₃. *Phys. Rev. B* **40**, 11927–11930 (1989).

94. R. Dronskowski, P. E. Bloechl, Crystal orbital Hamilton populations (COHP): Energy-resolved visualization of chemical bonding in solids based on density-functional calculations. *J. Phys. Chem.* **97**, 8617–8624 (1993).

95. V. L. Deringer, A. L. Tchougréeff, R. Dronskowski, Crystal orbital Hamilton population (COHP) analysis as projected from plane-wave basis sets. *J. Phys. Chem. A* **115**, 5461–5466 (2011).

96. S. Maintz, V. L. Deringer, A. L. Tchougréeff, R. Dronskowski, Analytic projection from plane-wave and PAW wavefunctions and application to chemical-bonding analysis in solids. *J. Comput. Chem.* **34**, 2557–2567 (2013).

97. K. Persson, M. Ekman, V. Ozolins, Phonon instabilities in bcc Sc, Ti, La, and Hf. *Phys. Rev. B* **61**, 11221–11224 (2000).

98. P. Hohenberg, W. Kohn, Inhomogeneous electron gas. *Phys. Rev.* **136**, B864–B871 (1964).

99. W. Kohn, L. J. Sham, Self-consistent equations including exchange and correlation effects. *Phys. Rev.* **140**, A1133–A1138 (1965).

100. G. Kresse, J. Furthmüller, Efficient iterative schemes for ab initio total-energy calculations using a plane-wave basis set. *Phys. Rev. B* **54**, 11169–11186 (1996).

101. P. E. Blöchl, Projector augmented-wave method. *Phys. Rev. B* **50**, 17953–17979 (1994).

102. G. Kresse, D. Joubert, From ultrasoft pseudopotentials to the projector augmented-wave method. *Phys. Rev. B* **59**, 1758–1775 (1999).

103. J. P. Perdew, K. Burke, M. Ernzerhof, Generalized gradient approximation made simple. *Phys. Rev. Lett.* **77**, 3865–3868 (1996).

104. M. Methfessel, A. T. Paxton, High-precision sampling for Brillouin-zone integration in metals. *Phys. Rev. B* **40**, 3616–3621 (1989).

105. P. E. Blochl, O. Jepsen, O. K. Andersen, Improved tetrahedron method for Brillouin-zone integrations. *Phys. Rev. B* **49**, 16223–16233 (1994).

106. A. Togo, I. Tanaka, First principles phonon calculations in materials science. *Scr. Mater.* **108**, 1–5 (2015).

107. A. van de Walle, P. Tiwary, M. de Jong, D. Olmsted, M. Asta, A. Dick, D. Shin, Y. Wang, L.-Q. Chen, Z.-K. Liu, Efficient stochastic generation of special quasirandom structures. *Calphad* **42**, 13–18 (2013).

108. D. Rodney, L. Ventelon, E. Clouet, L. Pizzagalli, F. Willaime, Ab initio modeling of dislocation core properties in metals and semiconductors. *Acta Mater.* **124**, 633–659 (2017).

109. E. Clouet, "Ab initio models of dislocations" in *Handbook of Materials Modeling*, W. Andreoni, S. Yips, Eds. (Springer International Publishing, 2018), pp. 1503–1524.

110. E. Clouet, Babel package (2023); http://emmanuel.clouet.free.fr/Programs/Babel.

111. P. Blonski, A. Kiejna, Calculation of surface properties of bcc iron. *Vacuum* **74**, 179–183 (2004).

112. S. Xu, Y. Su, L. T. W. Smith, I. J. Beyerlein, Frank-Read source operation in six body-centered cubic refractory metals. *J. Mech. Phys. Solids* **141**, 104017 (2020).

113. F. Birch, Finite elastic strain of cubic crystals. *Phys. Rev.* **71**, 809–824 (1947).

114. F. Murnaghan, *Finite Deformation of an Elastic Solid* (Wiley, 1951).

115. R. Gröger, Origin of variable propensity for anomalous slip in body-centered cubic metals. *Model. Simul. Mater. Sci. Eng.* **30**, 085007 (2022).

116. L. Gimeno Fabra, *Designs, Manufacture and Properties of Cr-Re Alloys for Apllication in Satellite Thrusters* (Universitat Politècnica de Catalunya, 2006).

117. E. Fazakas, V. Zadorozhnyy, L. K. Varga, A. Inoue, D. V. Louzguine-Luzgin, F. Tian, L. Vitos, Experimental and theoretical study of Ti₂₀Zr₂₀Hf₂₀Nb₂₀X₂₀ (X = V or Cr) refractory high-entropy alloys. *Int. J. Refract. Met. Hard Mater.* **47**, 131–138 (2014).

118. F. G. Coury, M. Kaufman, A. J. Clarke, Solid-solution strengthening in refractory high entropy alloys. *Acta Mater.* **175**, 66–81 (2019).

119. O. N. Senkov, S. Rao, K. J. Chaput, C. Woodward, Compositional effect on microstructure and properties of NbTiZr-based complex concentrated alloys. *Acta Mater.* **151**, 201–215 (2018).

120. O. N. Senkov, S. V. Senkova, D. B. Miracle, C. Woodward, Mechanical properties of low-density, refractory multi-principal element alloys of the Cr-Nb-Ti-V-Zr system. *Mater. Sci. Eng. A* **565**, 51–62 (2013).

121. N. N. Guo, L. Wang, L. S. Luo, X. Z. Li, R. R. Chen, Y. Q. Su, J. J. Guo, H. Z. Fu, Effect of composing element on microstructure and mechanical properties in Mo-Nb-Hf-Zr-Ti multi-principle component alloys. *Intermetallics* **69**, 13–20 (2016).

122. S. Maiti, W. Steurer, Structural-disorder and its effect on mechanical properties in single-phase TaNbHfZr high-entropy alloy. *Acta Mater.* **106**, 87–97 (2016).

123. L. Xu, Y. Jia, S. Wu, Y. Mu, Y. Jia, G. Wang, Low cycle fatigue properties of refractory high-entropy HfNbTiZr alloy. *Intermetallics* **152**, 107751 (2023).

124. H. Huang, Y. Wu, J. He, H. Wang, X. Liu, K. An, W. Wu, Z. Lu, Phase-transformation ductilization of brittle high-entropy alloys via metastability engineering. *Adv. Mater.* **29**, 201701678 (2017).

125. Y. Zhang, X. Yang, P. K. Liaw, Alloy design and properties optimization of high-entropy alloys. *JOM* **64**, 830–838 (2012).

126. Z. D. Han, N. Chen, S. F. Zhao, L. W. Fan, G. N. Yang, Y. Shao, K. F. Yao, Effect of Ti additions on mechanical properties of NbMoTaW and VNbMoTaW refractory high entropy alloys. *Intermetallics* **84**, 153–157 (2017).

127. H. W. Yao, J. W. Qiao, J. A. Hawk, H. F. Zhou, M. W. Chen, M. C. Gao, Mechanical properties of refractory high-entropy alloys: Experiments and modeling. *J. Alloys Compd.* **696**, 1139–1150 (2017).

128. S.-P. Wang, J. Xu, TiZrNbTaMo high-entropy alloy designed for orthopedic implants: As-cast microstructure and mechanical properties. *Mater. Sci. Eng. C* **73**, 80–89 (2017).

129. H. Yao, J.-W. Qiao, M. Gao, J. Hawk, S.-G. Ma, H. Zhou, MoNbTaV medium-entropy alloy. *Entropy* **18**, 189 (2016).

130. S. Chen, X. Yang, K. Dahmen, P. Liaw, Y. Zhang, Microstructures and crackling noise of AlₓNbTiMoV high entropy alloys. *Entropy* **16**, 870–884 (2014).

131. D. X. Qiao, H. Jiang, X. X. Chang, Y. P. Lu, T. J. Li, Microstructure and mechanical properties of VTaTiMoAlₓ refractory high entropy alloys. *Mater. Sci. Forum* **898**, 638–642 (2017).

132. H. W. Yao, J. W. Qiao, M. C. Gao, J. A. Hawk, S. G. Ma, H. F. Zhou, Y. Zhang, NbTaV-(Ti, W) refractory high-entropy alloys: Experiments and modeling. *Mater. Sci. Eng. A* **674**, 203–211 (2016).

133. O. N. Senkov, S. V. Senkova, C. Woodward, D. B. Miracle, Low-density, refractory multi-principal element alloys of the Cr-Nb-Ti-V-Zr system: Microstructure and phase analysis. *Acta Mater.* **61**, 1545–1557 (2013).

134. J. Liu, Y. Huang, W. Liu, Y. Wang, Y. Zhang, Y. Ma, Effect of tantalum concentration on the microstructure and mechanical properties of novel W-Ta-Re alloy. *Vacuum* **207**, 111627 (2023).